

Improved Oxygen Redox Activity by High-Valent Fe and Co³⁺ Sites in the Perovskite LaNi_{1-x}Fe_{0.5x}Co_{0.5x}O₃

Anjaiah Sheelam, Sakthipriya Balu, Adil Muneeb, Khasim Saheb Bayikadi, Dhenadhayalan Namasivayam, Erakulan E. Siddharthan, Arif I. Inamdar, Ranjit Thapa, Ming-Hsi Chiang, Song-Jeng Isaac Huang, and Raman Sankar*



Cite This: *ACS Appl. Energy Mater.* 2022, 5, 343–354



Read Online

ACCESS |



Metrics & More



Article Recommendations

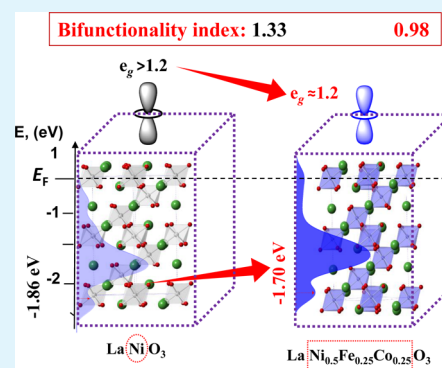


Supporting Information

ABSTRACT: Tuning the electronic structure of perovskite oxides via aliovalent substitution is a promising strategy to attain inexpensive and efficient electrocatalysts for energy conversion and storage devices. Herein, following the d-band center positions and using a simple sol–gel method followed by a pyrolysis step, LaNi_{1-x}Co_{0.5x}Fe_{0.5x}O₃ (LNFCO-*x*; *x* = 0.0, 0.4, 0.5, and 0.6) electrocatalysts are designed and synthesized for oxygen redox reactions in 1 M KOH. Among them, LNFCO-0.5 has exhibited the lowest overpotential and the highest charge transfer kinetics in oxygen redox reactions. Overall, a 90 mV lower overpotential was observed in oxygen redox activity of LNFCO-0.5 compared to that of pristine LaNiO₃. The mass activity of LNFCO-0.5 in the oxygen reduction reaction (at 0.7 V vs RHE) and oxygen evolution reaction (1.60 V vs RHE) was calculated to be 2.5 and 2.13 times higher than that of LaNiO₃, respectively. The bifunctionality index (potential difference between the oxygen evolution at a current density of 10 mA cm⁻² and the oxygen reduction at a current density of -1 mA cm⁻²) of LNFCO-0.5 was found to be 0.98.

The substitution of Fe and Co for the Ni-site shifted the d-band center close to the Fermi level, which can increase the binding strength of the *OH intermediate in the rate-determining step. Also, the surface was enriched with Fe^{3+Δ}, Co³⁺, and partially oxidized Ni³⁺ states, which is susceptible to tune the e_g-orbital filling for superior oxygen redox activity.

KEYWORDS: d-band center, e_g-orbital filling, oxygen evolution reaction, oxygen reduction reaction, bifunctional catalysts



1. INTRODUCTION

The alarming effects of global warming and the energy crisis have motivated researchers toward sustainable energy conversion and storage technologies.¹ Electrolyzers and rechargeable metal–air batteries offer a viable solution for environmental issues and growing energy demands by storing intermittent renewable energy in the form of hydrogen and chemicals.^{2,3} Particularly, Zn–air batteries offer 4–5 times higher energy density (1085 W h kg⁻¹) than the Li-ion batteries (200–250 W h kg⁻¹).³ The efficiency of the devices depends on the activity of oxygen redox reactions, namely oxygen reduction reaction (ORR, O₂ + 2H₂O + 4e⁻ → 4OH⁻ at E° = 0.401 V vs SHE) and oxygen evolution reaction (OER, which is the reverse reaction path of the ORR).⁴ The ORR and OER involve a complex and multi-electron transfer mechanism, which sets a high kinetic barrier for the oxygen redox reactions.^{5,6} Consequently, a large overpotential is required to drive these reactions, leading to the high “bifunctionality index” (BI) and poor efficient devices.⁷ The BI is a metric for oxygen redox activity defined as the potential difference between the OER and ORR at a specific current density. The well-known benchmark catalyst Pt shows high ORR kinetics but poor OER activity (*in situ* formed insulating Pt–O is

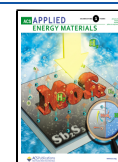
inactive for the OER),^{6,8} whereas RuO₂ and IrO₂ perform high OER and poor ORR activities (*in situ* formed high-valent oxide is inactive for ORR).⁹ One may notice that all these catalysts are noble and rare in the earth’s crust.¹⁰ As a result, they are prohibitively expensive and scarcely employed in large-scale production.¹¹ To end this, redox-active transition metal-based nonprecious metal catalysts (perovskites, 2D-layers, metal–nitrogen–carbons, metal–complexes, metal–organic frameworks, and coordination polymers) are emerging as potential alternative catalysts for oxygen redox reactions.^{12–23}

Perovskites are unique materials in which vast composition adjustability (90% of elements present in the periodic table can be utilized) and the interplay between the lattice, orbital, charge, and spin degree of freedom leads to exotic phenomena and diverse applications.^{24–29} The general formula of perov-

Received: September 15, 2021

Accepted: December 7, 2021

Published: January 7, 2022



skite oxides is “ABO₃”, where A is the rare-earth or alkaline-earth metal and B is the transition metal. The high Goldschmidt tolerance factor of perovskites allows the isovalent and aliovalent doping that opened the tunability in electrocatalytic properties.^{25,30,31} Computational studies suggested that the perovskites containing La at the A-site and first-row transition metals (Mn, Fe, Co, or Ni) at the B-site are promising electrocatalysts for oxygen redox reactions.^{32–34} Particularly, LaNiO₃ (LNO) has been attracting interest as an efficient and inexpensive electrocatalyst because of its highly conductive metallic state (Ni³⁺-site, $t_{2g}^6 e_g^1$) and promising oxygen redox activities.³⁵ However, the BI is too large, 1.33 V, to meet the practical requirements of metal–air batteries. The property which bridges the observed electrocatalytic activity and intrinsic electronic structure of the catalyst is the binding strength of reaction intermediates of the ORR and/or OER. Furthermore, the electronic structure descriptors, such as e_g -orbital filling, 3d–2p hybridization, the O 2p band center, and charge-transfer energy, were proposed to correlate the ORR and/or OER.^{34,36–38} The A-site deficiency in La_{1–x}NiO₃ is found to decrease the BI due to the improved hybridization between Ni-3d and O-2p orbitals.³⁶ However, excess oxygen vacancies lead to structural distortion and generate an electrically insulating NiO phase, which is unfavorable to the OER activity.^{36,39} A similar issue was reported in La_{1–x}FeO₃ and La_{1–x}CoO₃ structures, where Fe₂O₃ and Co₃O₄ are formed as the nonperovskite phases.^{40,41} The aliovalent substitution of Fe for the Ni-site in LaNi_{0.8}Fe_{0.2}O₃ enhanced the OER activity by stabilizing the surface Ni³⁺ with Fe³⁺.⁴⁰ The optimum substitution of Ni³⁺-sites for Co (LaCo_{0.5}Ni_{0.5}O₃) resulted in the mixed-valence states of Ni³⁺/Ni²⁺ and Co³⁺/Co²⁺ and synergistically optimized the OH adsorption and O₂ desorption ability.⁴¹ Suntivich et al. reported a volcano-type relationship between OER activity and e_g -orbital filling of transition metals. The deprotonation of adsorbed OH species (*OH) to *O is reported as the rate-determining step (rds) in the OER on LNO.³⁴ Recently, the active role of higher oxidation states of Fe and Co (higher than the usual 3+ valency) in perovskites is attracting interest as potential sites for oxygen redox reactions.^{42–45} Yagi et al. reported an unusual high-valent Fe⁴⁺-based quadruple CaCu₃Fe₄O₁₂ (CCFO) perovskite as a highly active OER electrocatalyst.⁴⁶ The OER activity of CCFO is surprisingly higher than that of the other Fe⁴⁺-based perovskites, SrFeO₃ (Fe–O–Fe, ~180°) and CaFeO₃ (Fe–O–Fe, ~157.9°), and Ba_{0.5}Sr_{0.5}Co_{0.5}Fe_{0.5}O_{3–δ}.^{47–49} The strained Fe–O–Fe (~140°) bonds facilitated the Langmuir–Hinshelwood-type reaction mechanism through the direct O–O bond formation (without the deprotonation of *OOH to *OO^{2–} formation) between the neighboring two nearest Fe–O^{2–} sites (~2.6 Å).

Here, we employed the density functional theory (DFT) calculations to find the d-band center (E_d) of LNFCO-*x* (*x* = 0.0, 0.2, 0.4, 0.5, and 0.6). Based on E_d , we synthesized a series of LaNi_{1–x}Co_{0.5x}Fe_{0.5x}O₃ (LNFCO-*x*; *x* = 0.0, 0.4, 0.5, and 0.6) via a facile sol–gel method followed by pyrolysis and evaluated their ORR and OER activities in 1 M KOH electrolyte. Careful X-ray photoelectron spectroscopy (XPS) studies were used to identify valences of Ni (2+ and 3+), Co (2+ and 3+), and Fe (3+ and (3+Δ)) and their relative distribution on the surface of LNFCO-*x* (*x* = 0.4, 0.5, and 0.6) that can alter the e_g -orbital filling toward an ideal value ($e_g \approx 1.2$). The presence of higher oxidation states Fe^{3+Δ} and Co³⁺ at the Ni-site significantly improved the BI of LNFCO-0.5 from 1.33 to 0.98 V.

2. EXPERIMENTAL SECTION

2.1. Materials. Lanthanum(II) nitrate hexahydrate (La(NO₃)₂·6H₂O), iron nitrate nonahydrate (Fe(NO₃)₃·9H₂O), cobalt hexahydrate (Co(NO₃)₂·6H₂O), nickel hexahydrate (Ni(NO₃)₂·6H₂O), and Toray carbon cloth (0.37 mm) were purchased from Alfa Aesar. 5 wt % Nafion ionomer solution, 20 wt % Pt/C, IrO₂, Zn foil (0.2 mm), polyvinyl alcohol (PVA, mw: 195,000), polyethyleneglycol (PEG, mw: 20,000), and SiO₂ (50 nm) were procured from Sigma-Aldrich, USA. Ketjenblack EC-600JD carbon (Akzo Nobel, USA) was utilized as obtained. Citric acid was obtained from Acros Organics (Geel, Belgium). High-pure O₂ and N₂ cylinders were supplied by Shinn Hwa Gas Co. LTD, Taiwan. Ultrapure water (18.2 MΩ cm) was collected from a Milli-Q ultrapure system purchased from Merck Millipore (Billerica, MA, USA).

2.2. Computational Details. All the structural optimization calculations are performed in the Vienna ab-initio simulation package (VASP) and electronic structure calculations in the Quantum Espresso package using spin-polarized DFT.^{50,51} The projected augmented wave (PAW) method is used to describe the potentials of the atoms, and generalized gradient approximation (GGA) is considered for the exchange and correlation effects at the Perdew–Burke–Ernzerhof (PBE) level.^{52,53} A plane-wave cut-off energy of 450 eV is used for the calculations. The Monkhorst–Pack scheme with a 5 × 5 × 1 K-point grid is used for the Brillouin zone sampling for structural optimizations with 9 × 9 × 1 for electronic structure calculations. Structural optimizations were carried out until the total energy converged less than 10–4 eV per atom and the maximum force converged less than 10–3 eV/Å. A 2 × 2 model of the LNO structure is taken, which is cleaved in the [110] direction. The last layer of metal and oxygen atoms was fixed during the optimization studies. The Ni-site (shown in Figure S1) is selected as an active site, and Fe and Co are doped in varying concentrations around the Ni-site to evaluate the effect of substitution. A vacuum of 15 Å is taken in the Z-direction to avoid periodic interactions.

2.3. Synthesis of LNFCO-*x* (*x* = 0.0, 0.4, 0.5, and 0.6). A facile sol–gel method was used to synthesize LNFCO-*x* (*x* = 0.0, 0.4, 0.5, and 0.6) materials. A total of 2 mmol La(NO₃)₂·6H₂O and 2 mmol Ni(NO₃)₂·6H₂O were dissolved in 30 mL of ultrapure water followed by the slow addition of 3 mmol citric acid. The mixture was heated to 90 °C under slow stirring to form a viscous gel, which was then subjected to pre-calcination at 190 °C for 2 h in a hot air oven. At around 150 °C, the samples were suddenly ignited for few seconds and converted into a delicate foam-like structure. The dry amorphous precursor thus formed was grounded using a mortar and pestle. Then, the precursor powder was calcined at 800 °C for 6 h with an heating rate of 1 ° min^{–1} in an ambient atmosphere to remove the residual carbon and to form the crystalline LaNiO₃. The same procedure was repeated to prepare LNFC (*x* = 0.4, 0.5, and 0.6) with appropriate amounts of Co(NO₃)₂·6H₂O and Fe(NO₃)₂·9H₂O.

2.4. Characterization Methods. The X-ray diffraction (XRD) patterns were recorded using a Bruker-D8 Advance facility fitted with a Cu Kα X-ray source (1.5418 Å). The scanning electron microscopy (SEM) images were obtained using a Hitachi S4800 HR-SEM instrument. High-resolution transmission electron microscopy (HR-TEM), JSM-1200EX II, was employed to measure the size of perovskite nanomaterials and their selected area electron diffraction (SAED) patterns. A VG ECSA250 electron microscope from VG scientific (West Sussex, UK) was employed for XPS measurements of the catalysts. The electrochemical measurements were performed employing Autolab PGSTAT302N. The rotating disc electrode (RDE) polarization curves and rotating ring-disc electrode (RRDE) analysis were processed using Autolab PGSTAT302N coupled with PINE Research Instruments, USA. The amount of Ni, Co, and Fe leached into the 1 M KOH was estimated using inductively coupled plasma optical emission spectrometry (ICP-OES), Perkin Elmer Optima 5300 DV.

2.5. Electrode Preparation for ORR Testing. First, RDE and RRDE electrodes were polished with alumina slurries of 50 nm on a polishing pad followed by 2 min of ultrasonication in ultrapure water.

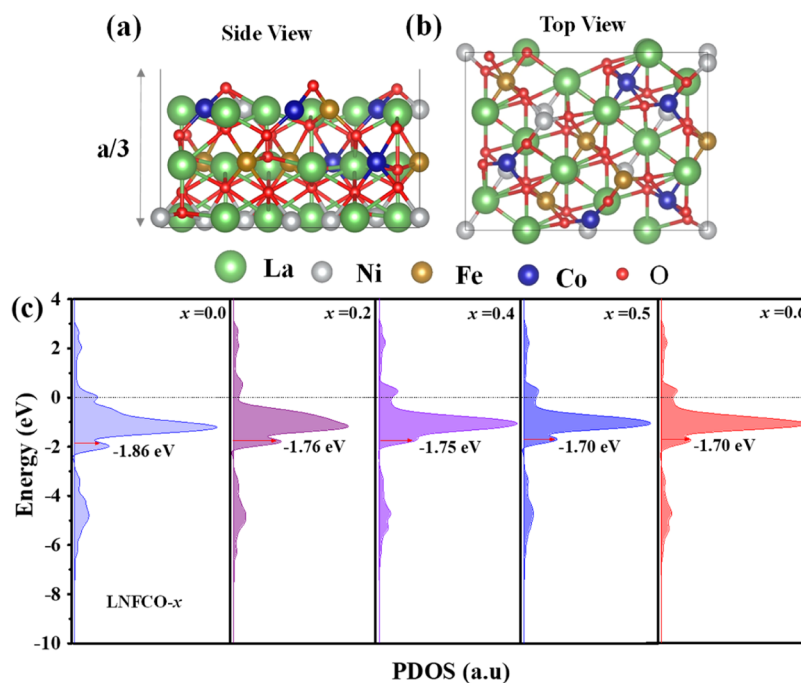


Figure 1. (a) and (b) Side and top views of the optimized structure of the LNFCO-0.5, respectively, and (c) PDOS of LNFCO- x ($x = 0.0, 0.2, 0.4, 0.5,$ and 0.6) (Fermi level is at 0, and the d-band center is shown in the red arrow).

Then, the electrodes were dried in a hot air oven at 50 °C before drop-casting the catalyst ink. A total of 10 mg of the sample was dissolved in a mixed solvent of isopropyl alcohol and ultrapure water (1.5 mL + 0.48 mL) containing 20 μL of 5 wt % Nafion and ultrasonicated for 1 h to obtain a homogeneous ink-like dispersion. A total of 7.8 μL of the catalyst (200 $\mu\text{g cm}^{-2}$) ink was drop-casted onto a 5 mm-diameter glassy carbon electrode of the or the disc part of the RRDE and dried at room temperature.

2.6. Electrochemical Measurements. All the electrochemical measurements were carried out using a three-electrode setup at room temperature, containing a 5 mm RDE or RRDE as a working electrode, Ag/AgCl (sat. KCl, ~ 3.8 M at 25 °C) electrode as a reference electrode, and graphite rod (15 \times 6 mm length and diameter) as a counter electrode in 1 M KOH electrolyte. The inner and outer diameter of the Pt ring of the RRDE is 6.5 and 8.5 mm, respectively. The potentials applied against the Ag/AgCl reference electrode were converted to a reversible hydrogen electrode (RHE) according to $E(\text{V vs RHE}) = [E(\text{V vs Ag/AgCl}) + 0.198 \text{ V}] + (0.059 \times \text{pH})$. The electrolyte was saturated with high-pure N_2 or O_2 by purging the gas into the electrolyte for about 30 min, and the flow was maintained above the electrolyte while running the electrochemical measurements. The solution resistance was obtained from Randles circuit fitting to the electrochemical impedance spectrum data. The Randles circuit is an equivalent electrical circuit, which consists of solution resistance (R) in series to the parallel combination of the double-layer resistance (C_{dl}) and charge-transfer resistance (R_{ct}). RRDE analysis was carried out while scanning the catalyst-coated glassy carbon disc in the potential range of 1.0–0.15 V versus RHE. A Pt ring was applied with a potential of 1.30 V versus RHE to oxidize the HO_2^- intermediate. The ring potential was carefully selected to be positive to the ORR potential limit (>1.23 V vs RHE) and negative to the onset of the OER. The fraction of oxygen molecules reduced to peroxy ions ($\chi_{\text{HO}_2^-}$ in %) and the number of electrons (n) were derived from the ring and disk polarization currents using eqs 1 and 2, respectively.

$$\chi_{\text{HO}_2^-} = \frac{2[|i_{\text{ring}}|/C. E]}{|i_{\text{disk}}| + |i_{\text{ring}}|/C. E} \times 100 \quad (1)$$

$$n = \frac{4|i_{\text{disk}}|}{|i_{\text{disc}}| + |i_{\text{ring}}|/C. E} \quad (2)$$

where i_{ring} and i_{disk} stand for the ring current and disk current, respectively. The collection efficiency (C.E) of the RRDE was estimated to be 0.31 using the reported procedure.⁵⁴

2.7. Flexible Zn–Air Battery Fabrication. A 1 mm-thick Zn foil (1 \times 3 cm) was used as an anode, and a catalyst ink-coated carbon cloth (3 mg cm^{-2}) was used as a cathode for the battery fabrication. A 6 M KOH-soaked PVA gel membrane was prepared using a reported procedure with a slight modification.⁵⁵ Briefly, 150 mg of SiO_2 and 3 g of PVA were dissolved in ultrapure water and stirred at 80 °C to form a transparent viscous liquid. The solution thus formed was added dropwise to 50 mL of pore-forming agent (100 mg of PEG) containing acetone solution. The resultant solution was stirred for 10 h and poured into a 3 mm-deep plastic mold and kept at -10 °C for another 10 h to form a cross-linking polymer. The resultant membrane was immersed in ethanol (99.5%) to remove PEG and SiO_2 . The membrane thus prepared was soaked in 6 M KOH electrolyte for 24 h to get the final PVA gel membrane for the flexible Zn–air battery. A thin copper tape was used as current leads, and the membrane–electrode assembly was sealed in an acrylic polymer sheet.

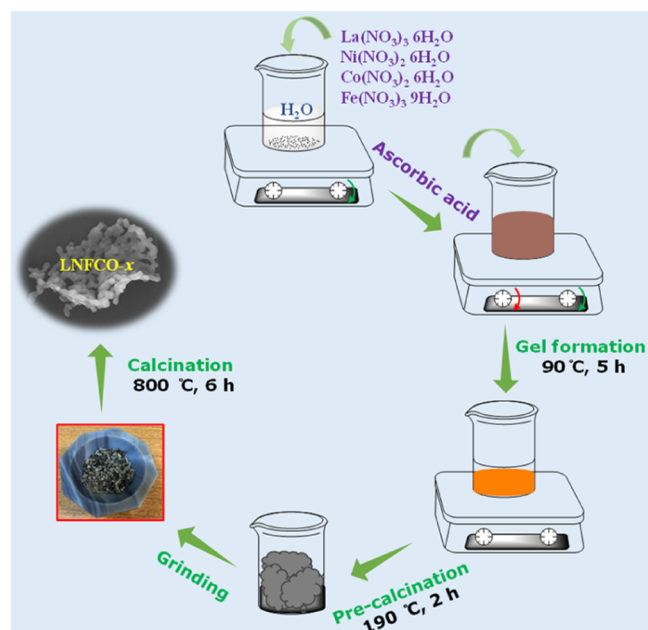
3. RESULTS AND DISCUSSION

3.1. Catalyst Design from DFT Calculations. Structures of pristine LNO and LNFCO- x ($x = 0.2, 0.4, 0.5,$ and 0.6) were optimized using DFT calculations. Figures 1a,b, and S1a,b show the side and top view of DFT-optimized structures of LNFCO-0.5 and LNO, respectively. Furthermore, the projected density of states (PDOS) and E_d were calculated to predict the oxygen redox activities. The oxygen redox activity of LNO is unsatisfactory for the practical application of rechargeable metal–air batteries. The d-band theory correlates the electrocatalytic activity (HER, ORR, and/or OER) and adsorption energies of reaction intermediates ($^*\text{OH}$, $^*\text{O}$, and $^*\text{OOH}$) by considering the intrinsic electronic structure of the catalyst.^{52–54} The energy difference between Fermi energy (E_F) and E_d proportionally contributes to the binding strength

of intermediates. Therefore, optimizing the electronic structure via doping can lead to the “not too strong” or “not too weak” binding strength of the intermediates. The E_d of LNO is found to be -1.86 eV, which is lower than that of the well-known efficient bifunctional catalysts. Therefore, weak binding of intermediates is anticipated with the catalyst surface, which could be the origin of high overpotential for oxygen redox reactions on LNO.^{7,56} The binding strength of *OH was facilitated by the partial substitution of Fe for Ni of LNO in oxygen redox reactions.^{14,57} We calculated the E_d of LNO by the substitution of the Ni-site ($1-x$) with both Co and Fe ($x = 0.5xCo + 0.5xFe$) in equal amounts. A line of different concentrations ($x = 0.2, 0.4, 0.5$, and 0.6) were chosen to identify the shift in E_d of LNFCO- x ($x = 0.0, 0.2, 0.4, 0.5$, and 0.6). The E_d of LNFCO- x ($x = 0.0, 0.2, 0.4, 0.5$, and 0.6) is calculated to be $-1.86, -1.78, -1.70$, and -1.70 eV, respectively (Figure 1c). The substitution of Fe and Co has resulted in a gradual shift (closer to E_F) in E_d . Therefore, the stronger binding strength of *OH and lower overpotential are expected in oxygen redox reactions.^{14,34,58,59}

3.2. Synthesis and Characterization of LNFCO- x ($x = 0.0, 0.4, 0.5$, and 0.6). Following the E_d , we have synthesized LNFCO- x ($x = 0.0, 0.4, 0.5$, and 0.6) as explained in the Experimental Section. The schematic of the synthesis is illustrated in Scheme 1. The powder XRD patterns of as-

Scheme 1. Schematic Representation of the Sol–Gel Method of Synthesis Followed by Calcination to Prepare the LNFCO- x ($x = 0.0, 0.4, 0.5$, and 0.6)



prepared LNFCO- x ($x = 0.0, 0.4, 0.5$, and 0.6) are presented in Figure 2a with an enlarged view of (012), (110), and (104) plane reflections. All the samples show a hexagonal structure with a space group of $R\bar{3}c$. The XRD pattern of LNO is well-matched with the reported diffraction data (JCPDS # 88-0633). Due to the substitution of Fe and Co at the Ni-site, the reflections of (012), (110), and (104) planes are shifted to lower angles, which implies the lattice expansion due to the larger ionic radius of Ni^{3+} (low spin, 6-coordination site, 0.56 Å) compared to that of Fe^{3+} (low spin, 6-coordination site, 0.55 Å) and Co^{3+} (low spin, 6-coordination site, 0.54 Å).⁶⁰

The intensity of the (104) plane reflection is comparable to that of the 100% peak, which shows the significant growth of LNFCO- x ($x = 0.5$ and 0.6) in the respective crystal facet. A constant intensity of small reflection at 2θ of 39° was identified as the NiO phase in LNFCO- x ($x = 0.0, 0.4, 0.5$, and 0.6). The lattice structures were further refined using the Rietveld method to extract the lattice parameters. The XRD thus fitted and refined structures are displayed in Figures S2 and S3, respectively. Figure 2b,c shows the (110) and (104) view of refined structures of LFCNO-0.5, respectively.

The cell parameters are summarized in Table S1. According to the calibrated parameters, the lattice structure of the measured composition is in good agreement with the reported LNO structure (84933-ICSD), signifying the phase purity of the material. The bond angle of B–O–B (where B = Ni or Ni/Fe/Co) is significantly higher in LNFCO-0.4 (170.66°), LNFCO-0.5 (169.56°), and LNFCO-0.6 (171.10°) materials compared to that of LNO (165.99°). The list of selected bond lengths and bond angles is shown in Table S2.

The morphologies of as-prepared LNFCO- x ($x = 0.0, 0.4, 0.5$, and 0.6) were scrutinized by SEM, and microimages thus obtained are shown in Figure S4. The microimages of LNO and LNFCO-0.4 look like agglomerates without a well-defined shape. However, the LNFCO- x ($x = 0.5$ and 0.6) particles are shaped into a well-formed net-like structure. It is also noted that the particle size of LNFCO-0.5 (~ 80 nm) decreased by approximately 20 nm from LNO (~ 100 nm). With further increasing the doping amount of Fe and Co (LNFCO-0.6), particle size is raised back to ~ 100 nm. The N_2 adsorption–desorption isotherms were obtained using a Micromeritics pore size analyzer (Figure S5). The nonporous nature of the samples was revealed through the type-II isotherm. The specific surface area of LNO is found to be 9.66 m²/g using the Brunauer–Emmett–Teller (BET) equation. The LNFCO-0.5 contains the highest BET surface area of 14.46 m²/g and the smallest particle size among all the samples. Therefore, LNFCO-0.5 can avail a large contact area between the electrolyte and active sites with a facile diffusion that would enable oxygen redox activity.

The electrical resistivity of the samples was measured between 27 and 60 °C using a PPMS instrument with an excitation current of 200 μA . The width of the pellets was 1 mm, and the distance between two voltage points was ~ 0.62 mm. The electrical conductivity (σ) was calculated using the resistivity values obtained from the PPMS measurement. Figure S6 shows the temperature versus conductivity plot for all the samples. The electrical conductivity of LNO is found to be 864 S cm^{-1} at 27 °C, which is comparable to the reported literature.⁶¹ The conductivity of LNO gradually decreased to 780 S cm^{-1} as the temperature increases to 60 °C, which revealed the metallic nature of LNO, whereas LNFCO- x ($x = 0.4, 0.5$, and 0.6) exhibited a gradual increase in the conductivity, indicating their semiconductor behavior. Table S3 lists the electrical conductivity (S cm^{-1}), unit cell volume (\AA^3), and BET surface area (m² g⁻¹) along with the charge-transfer resistance (R_{ct} , Ω) of the catalysts. The analysis of XRD, BET, and resistivity measurements indicates that the substitution of Fe and Co for Ni leads to a lower density material with decreased electrical conductivity. However, the electrical conductivity of the samples is few orders of magnitude higher than that of the usual carbon supports (volume resistivity of Ketjenblack carbon is 0.1 S cm^{-1} at 6 wt %, carbon black is 0.1 S cm^{-1} at 22 wt %, and acetylene carbon

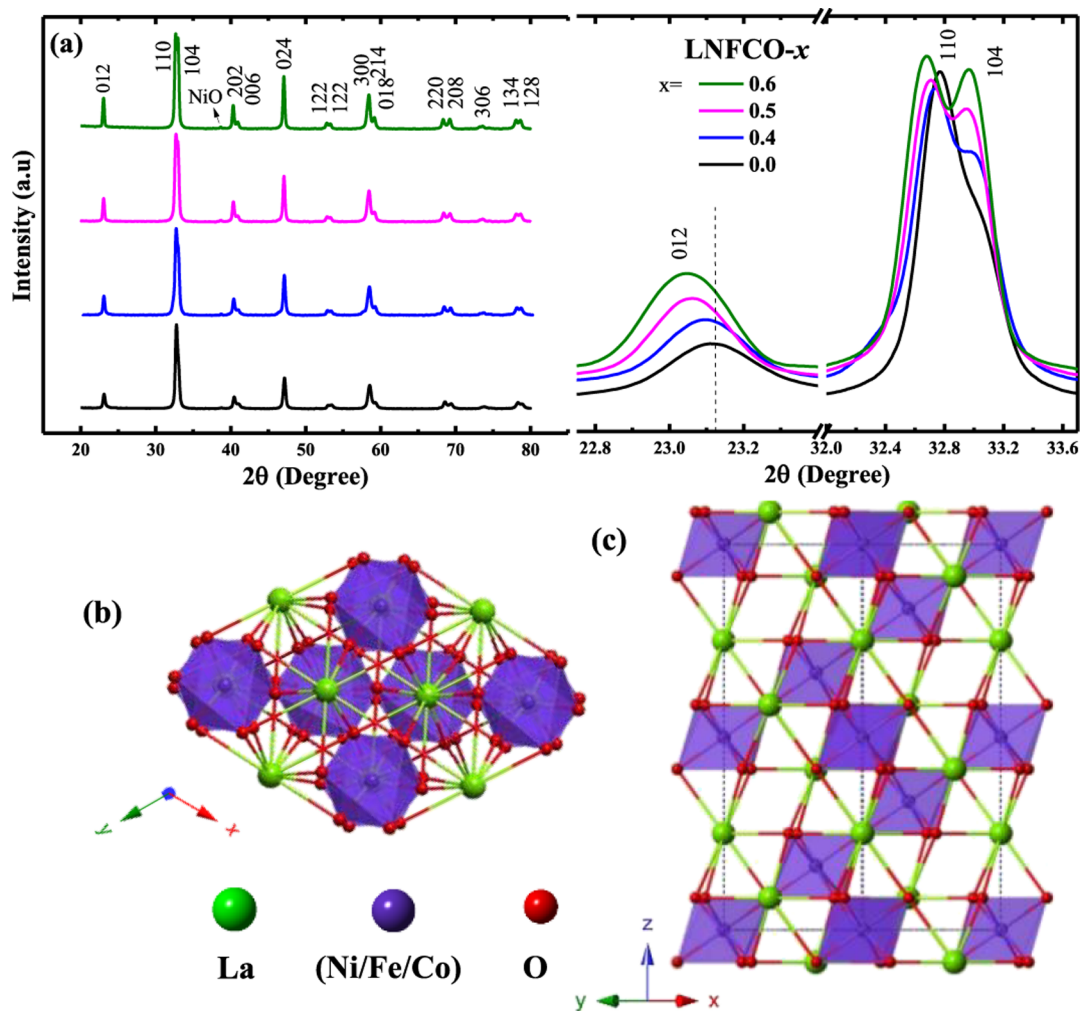


Figure 2. (a) Comparison of the XRD pattern of LNFCO- x ($x = 0.0, 0.4, 0.5,$ and 0.6) with an enlarged view of (012), (110), and (104) plane reflections and (b) (110) and (c) (104) plane views.

is 0.1 S cm^{-1} at 25 wt %) for electrocatalysts.⁶² The lower electrical conductivity of carbon can offer substantial impedance to the electron path via the Schottky barrier at the carbon–catalyst interface, which results in a high overpotential (Figure S7).⁶³ In the OER active potential regime ($>1.23 \text{ V}$ vs RHE), the corrosion of carbon is a known parasitic loss.⁶⁴ In addition, the insulating functionalities generated during carbon corrosion could potentially inhibit the OER durability. To avoid such negative impacts, as-synthesized materials were directly studied as electrocatalysts for oxygen redox reactions without any carbon addition.

HR-TEM was used to examine the LNFCO-0.5 nanomaterials at the nanolevel. As shown in Figure 3a,b, the LNFCO-0.5 net-like structure consists of hexagonal nanocrystals of various sizes ranging from 50 to 100 nm. The nanocrystal shows well-resolved lattice fringes with an interplanar distance of 0.29 nm at the basal plane and 0.27 nm at the edges, corresponding to (110) and (104) planes, respectively (Figure 3c,d). Figure 3e shows the SAED pattern obtained from the area highlighted in Figure 3b, which indicates the single-crystalline nature of hexagonal nanocrystals of LNFCO-0.5. Also, a uniform distribution of all constituent elements (La, Ni, Fe, Co, and O) was observed in the energy dispersion X-ray analysis (EDAX) elemental mapping, confirming the homogeneous substitution of Fe and Co at the Ni-site (Figure 3f–j).

3.3. ORR and OER Electrocatalytic Activity. The oxygen redox activity of LNFCO- x ($x = 0.0, 0.4, 0.5,$ and 0.6) in 1 M KOH was evaluated using linear sweep voltammetry (LSV), RDE, RRDE, and electrochemical impedance spectroscopy (EIS) experiments. Figure S8 shows the OER polarization curves of LNFCO-0.5 using a series of loadings, 100, 150, 200, and $250 \mu\text{g cm}^{-2}$, on the RDE at a scan rate of 10 mV s^{-1} . The lowest overpotential and highest current densities were observed at $200 \mu\text{g cm}^{-2}$ loading. Therefore, the same loading was continued to use throughout electrochemical studies. Figure 4a displays the iR -corrected (solution resistance, $R = 6 \Omega$) RDE polarization curves of all the catalysts obtained while rotating the electrode at 1600 rotations per minute (rpm) in O_2 -saturated 1 M KOH at a sweep rate of 10 mV s^{-1} and $25 \text{ }^\circ\text{C}$. We have also recorded the RDEs at different rotation speeds ranging from 100 to 1600 RPM (Figure S9). The increase in limiting current density as RPM increases signifies the diffusion limitation of O_2 to the electrode surface. The ORR onset potential on LNO is found to be 0.72 V versus RHE, and it is anodically shifted to approximately 55–60 mV on LNFCO- x ($x = 0.4, 0.5,$ and 0.6), implying the positive role of Fe and Co in the ORR activity. The highest half-wave potential (0.64 V vs RHE) of the LNFCO-0.5 shows its faster ORR kinetics compared to that of the other catalysts. It is important to note the effect of experimental factors on the

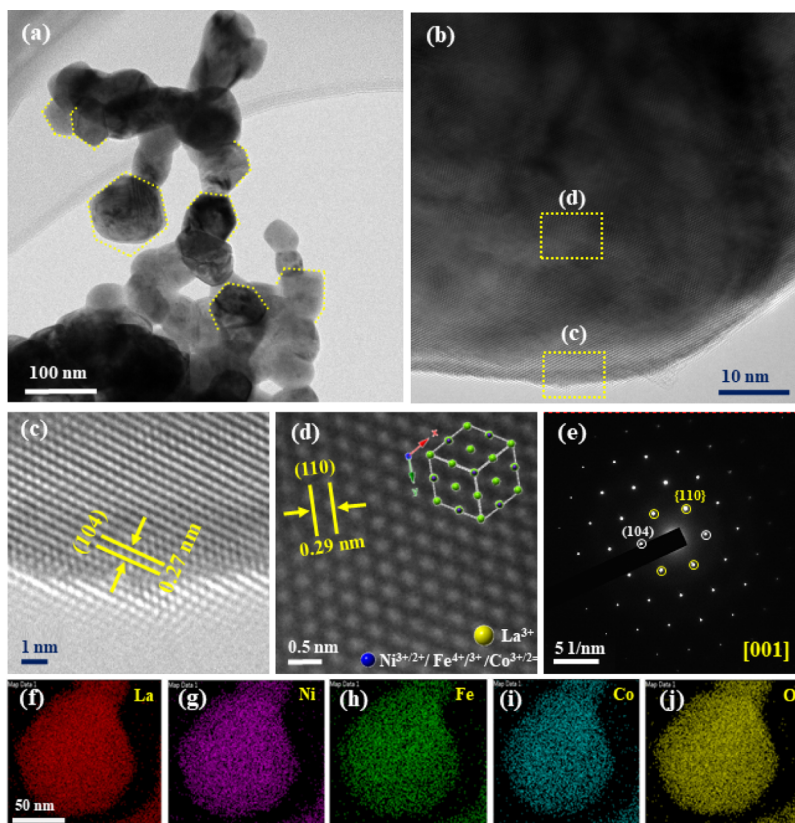


Figure 3. (a) and (b) HR-TEM images of LNFCO-0.5 and (c) and (d) its lattice fringes of (104) and (110); the plane obtained from the Rietveld refined structure is superimposed on the (110) plane, (e) SAED obtained from (c), and (f)–(j) elemental mappings of La, Ni, Fe, Co, and O, respectively.

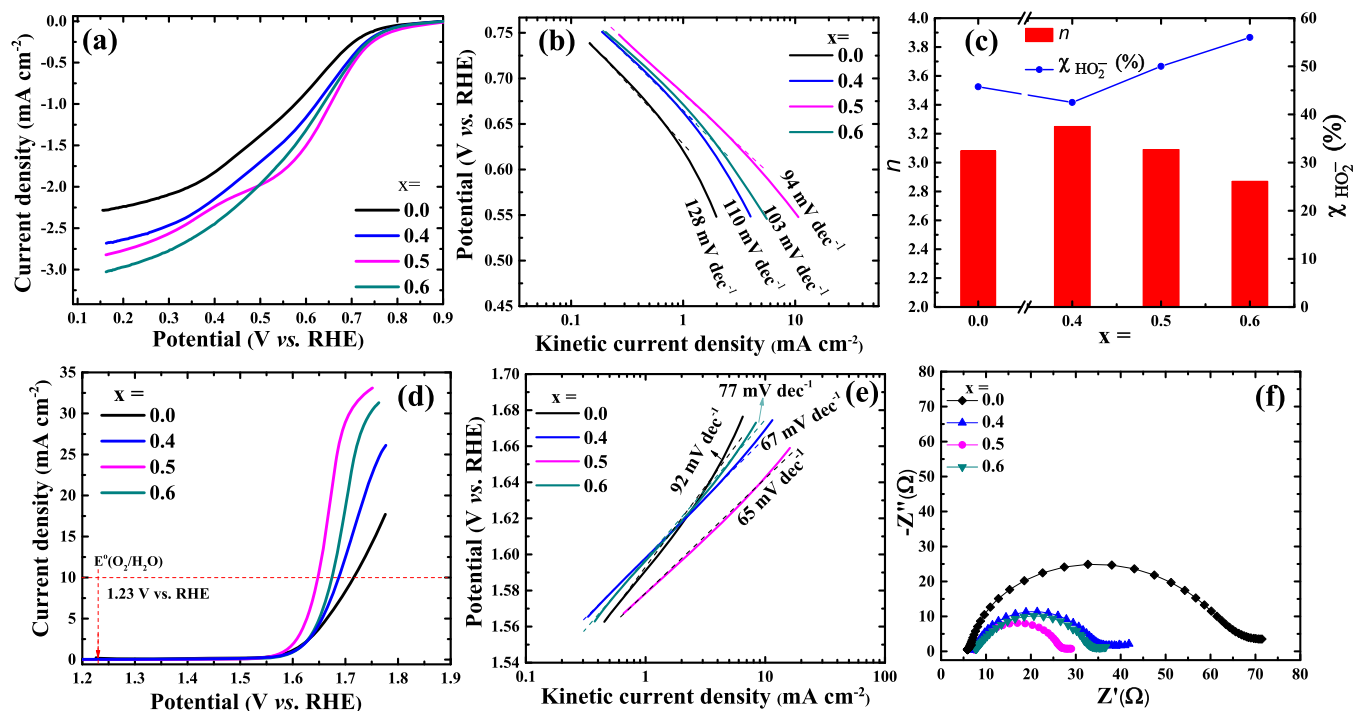


Figure 4. (a) ORR polarization curves of LNFCO- x ($x = 0.0, 0.4, 0.5,$ and 0.6) in 1 M KOH at a sweep rate of 10 mV s^{-1} and $25 \text{ }^\circ\text{C}$ and (b) their respective Tafel plots, (c) n and $\chi_{\text{HO}_2^-}$ derived from the RRDE experiment (I_{disk} and I_{ring} profiles shown in Figure S10), (d) OER LSVs and (e) their respective Tafel plots in the same electrolyte and conditions as in (a), and (f) EIS of LNFCO- x ($x = 0.0, 0.4, 0.5,$ and 0.6) electrodes carried out at 1.64 V versus RHE with a 10 mV of AC voltage perturbation.

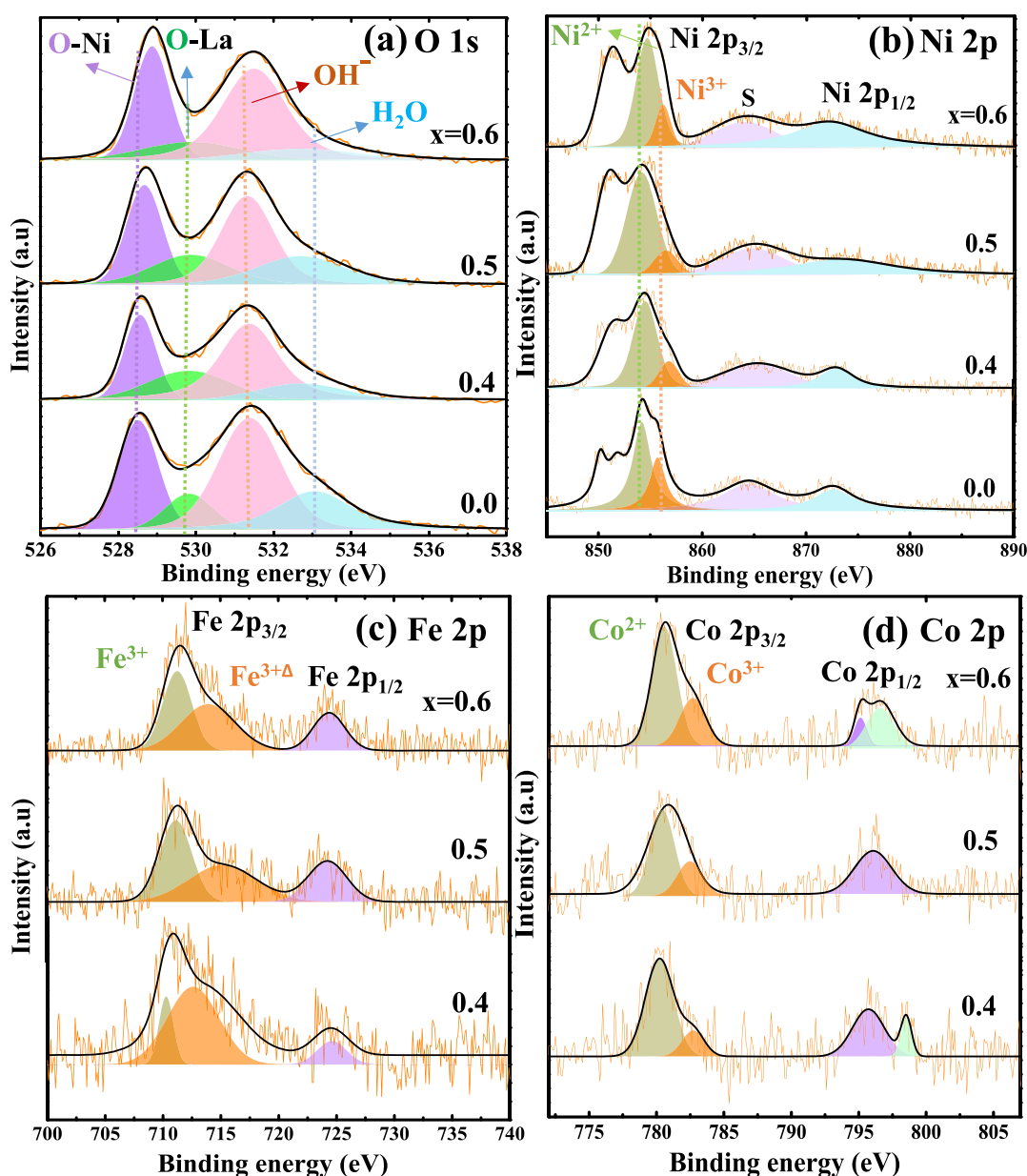


Figure 5. X-ray photoelectron spectra of (a) O 1s fitted with O–La and O–Ni, OH⁻, and H₂O species, (b) Ni 2p with 2+ and 3+, (c) Co 2p with 2+ and 3+, and (d) Fe 2p with 3+ and (3+Δ) valences on the surface of LNFCO-*x* (*x* = 0.0, 0.4, 0.5, and 0.6). “S” represents the satellite peaks.

deviation of limiting current density (i_{lim}) from theoretical values. The i_{lim} can be significantly altered by the O₂ flow conditions (the sand core tube is expected to improve the O₂ gas dissolution and diffusion to the electrode surface rather than a simple 3 mm tube), catalyst loading, flow rate, tightness of the electrochemical cell, electrolyte concentration, and purity.⁴³ Even though the ORR onset and half-wave potential of LNFCO-0.5 were higher than those of LNFCO-0.6, the i_{lim} is observed to be slightly low, which might be the result of relatively insufficient O₂ dissolution and diffusion to the improved active sites of the LNFCO-0.5 electrode surface.⁶⁵ Figure 4b shows the Tafel plot of LNFCO-*x* (*x* = 0.0, 0.4, 0.5, and 0.6) obtained from the iR - and mass-transfer-corrected ORR polarization curves. The Tafel slopes for LNFCO-*x* (*x* = 0.0, 0.4, 0.5, and 0.6) are calculated to be 128, 110, 94, and 103 mV dec⁻¹, respectively. The mass activity (MA) of the catalyst was calculated by normalizing the kinetic current density (i_k)

with the catalyst loading (i.e., 200 μg cm⁻²). The MA of LNFCO-*x* (*x* = 0.0, 0.4, 0.5, and 0.6) catalysts is 1.47, 2.64, 3.65, and 2.99 A g⁻¹ at 0.70 V_{iR-free} versus RHE, respectively. The lowest Tafel slope and highest MA of LNFCO-0.5 indicate its superior ORR kinetics compared to LNFCO-*x* (*x* = 0.0, 0.4, and 0.6). The n and χ_{HO_2} provide crucial information about the efficiency of electrocatalysts and the reaction pathways involved therein. To gain such insights into the ORR, RRDE analysis was carried out in N₂- and O₂-saturated 1 M KOH at a sweep rate of 10 mV s⁻¹ and 25 °C (Figure S10). Using eqs 1 and 2, the average n values and χ_{HO_2} for LNFCO-*x* (*x* = 0.0, 0.4, 0.5, and 0.6) are calculated to be 3.1, 3.3, 3.2, and 2.9 and 43, 45, 47, and 57%, respectively (Figure 4c). The increased dopings of Fe and Co (*x* = 0.6) catalyze the 2-electron pathway. A low overpotential and 4-electron pathway are the most desirable parameters for high-efficient fuel cells and rechargeable metal–air batteries.

Figure 4d shows the iR -corrected OER curves of LNFCO- x ($x = 0.0, 0.4, 0.5$ and 0.6) in 1 M KOH at 1600 RPM. The OER onset potential for LNFCO- x ($x = 0.0, 0.4$ and 0.6) is 1.57 V versus RHE. Among all the catalysts, LNFCO-0.5 exhibited the lowest onset potential of 1.57 V versus RHE and also the lowest overpotential of 410 mV (1.64 V vs RHE) at 10 mA cm⁻². To achieve the same current density (10 mA cm⁻²), the required overpotential on LNFCO- x ($x = 0.0, 0.4$, and 0.6) is observed to be 1.71, 1.69, and 1.67 V versus RHE, respectively. The MA of LNFCO-0.5 is 13 A g⁻¹ at 1.60 V _{iR -free} versus RHE, which is 2.13 times higher than that of the LNO (6.1 A g⁻¹) and also higher than that of the reported La_{1- x} NiO₃ (~7.2 A g⁻¹) and La_{1- x} FeO₃ (~6.2 A g⁻¹) catalysts.^{36,40} The MA of LNFCO- x ($x = 0.4$ and 0.6) is 5.2 and 5.7 A g⁻¹ at 1.60 V _{iR -free} versus RHE, respectively. Figure S11 compares the ORR and OER activities of LNFCO-0.5 with commercial 20 wt % Pt/C and IrO₂ catalysts. LNFCO-0.5 shows a 162 mV higher ORR overpotential compared to that of 20 wt % Pt/C at a current density of -1 mA cm⁻², whereas a 60 mV higher OER overpotential was noted compared to that of IrO₂ at 10 mA cm⁻². The methanol tolerance ORR activity of the cathode catalyst is an important factor for the direct methanol fuel cells. The crossover methanol from the anode chamber to the cathode can cause the mixed potential, which in turn lowers the cell potential. Therefore, we have also tested the oxygen redox activity of the LNFCO-0.5 catalyst with and without 1 M methanol in 1 M KOH (Figure S12). We did not observe any methanol oxidation peaks during the ORR (1.2 to 0.3 V vs RHE). Therefore, we can conclude that the LNFCO-0.5 is a potential cathode catalyst in direct methanol fuel cells. However, OER activity of the catalyst at 10 mA cm⁻² showed a 28 mV higher overpotential compared to that of the methanol-free 1 M KOH electrolyte. As shown in Figure 4e, the LNFCO-0.5 displays a lower Tafel slope of 65 mV dec⁻¹ compared to that of the LNO (92 mV dec⁻¹), LNFCO-0.4 (67 mV dec⁻¹), and LNFCO-0.6 (77 mV dec⁻¹), which signifies the excellent OER catalytic activity of LNFCO-0.5. Figure 4e shows the EIS plot of LNFCO- x ($x = 0.0, 0.4, 0.5$, and 0.6) catalysts, where Z' and Z'' represent the real and imaginary parts of the impedance, respectively. The charge-transfer resistance (R_{ct}) of LNFCO-0.5 (26 Ω) is lower than that of the LNO (66 Ω), LNFCO-0.4 (38 Ω), and LNFCO-0.6 (34 Ω) (Figure 4f). The lowest R_{ct} for the OER of LNFCO-0.5 confirms its superior intrinsic catalytic activity. Therefore, it should be noted that the increased MA of LNFCO-0.5 is not the sole result of the high BET surface area or the lower size, but it is mainly from the intrinsic catalytic property. The electrocatalytic activity of LNFCO- x ($x = 0.0, 0.4, 0.5$, and 0.6) in both the ORR and OER was compared with that of the related catalysts reported in the literature and is listed in Table S4. To assess the oxygen redox activity of the catalysts, the difference between the potentials of the OER at a current density of 10 mA cm⁻² and the ORR at -1 mA cm⁻² was calculated according to the equation $\Delta E = E_{i10, OER} - E_{i-1, ORR}$. This value is known as BI. The BI can be employed as a measure to select the suitable catalyst for practical applications in energy storage and conversion systems. A catalyst with a smaller BI can be considered as a better anode/cathode material for energy-efficient rechargeable metal-air batteries. The BI for LNFCO- x ($x = 0.0, 0.4, 0.5$, and 0.6) is 1.33, 1.12, 0.98, and 1.12, respectively. The BI of LNFCO-0.5 is smaller than that of the several reported catalysts and comparable to that of the best perovskite catalysts in the litera-

ture.^{36,40,41,57,66-70} Table S3 compares the onset potential of the ORR, OER, and BI of LNFCO-0.5 with reported perovskites. The oxygen redox reactions are the surface processes. Hence, not only the bulk properties such as E_d but also the surface cation distribution could significantly alter the electronic structure of the catalyst and its electrocatalytic activity. Therefore, it is of utmost importance to study the surface metal-ion valences and their relative amounts to reveal the smaller BI of LNFCO-0.5.

3.4. Surface Cation Distribution and e_g-Orbital Filling. The oxidation states of Ni, Fe, and Co and their relative abundance were investigated by XPS. The survey spectra of as-synthesized catalysts confirm the presence of La, Ni, Co, Ni, C, and O elements (Figure S13). Although the carbon material was not added to the samples, the survey spectra displayed the presence of a carbon peak at 285.08 eV. The potential source for the presence of carbon could be the residual carbon formed from the citric acid (which is a coordination agent for the metal ions in the synthesis procedure) during the pyrolysis process at 800 °C (Scheme 1). Figure 5a-d shows the comparison of XPS spectra of O 1s, Ni 2p, Co 2p, and Fe 2p with fitted valences present in LNFCO- x ($x = 0.0, 0.4, 0.5$, and 0.6). Figure 5a shows the O 1s spectra of all the catalysts. The surface oxygenated species of perovskite oxides are mainly categorized into two types, (i) lattice oxygen (O_{lat}), which includes the oxygen coordinated to La (O-La) and Ni (O-Ni), and (ii) adsorbed oxygenated groups (O_{ads}), such as chemically adsorbed OH⁻ species and physically adsorbed H₂O.^{57,71} The O 1s spectra of LNFCO- x ($x = 0.0, 0.4, 0.5$, and 0.6) are deconvoluted into four peaks. The lower binding energy peaks, 528.51 and 529.82 eV, are assigned to the O-Ni and O-La, respectively. The higher binding energy peaks, 531.38 and 533.08 eV, are ascribed to the adsorbed OH⁻ and H₂O, respectively. The area under the XPS peaks was calculated and attributed to their relative amounts. The O_{ads}/O_{lat} ratio lowered after the substitution of Fe and Co, indicating the decrease in adsorbed OH⁻ species and H₂O molecules on the surface of the catalysts. The increase in the O_{ads}/O_{lat} ratio in combination with O-Ni/O-La has been reported as crucial evidence for the O-vacancies in the structure of perovskite oxides.³⁶ Moreover, the slight increase in the binding energy of O-Ni accompanied by the decrease in the intensity of the O-La peak indicates the O-vacancy. Figure 5a did not exhibit such features in LNFCO- x ($x = 0.0, 0.4, 0.5$, and 0.6), which indicates the absence of significant O-vacancies. The relative increase in O-Ni peak intensity compared to that of the O_{ads} can be attributed to the presence of the NiO secondary phase, which is observed as a small peak in the XRD patterns (Figure 1). Figure 5b displays the Ni XPS spectra of LNFCO- x ($x = 0.0, 0.4, 0.5$, and 0.6). The binding energy of La 3d_{3/2} is partially overlapped with the Ni 2p_{3/2} (Figure 5b). To calculate the Ni valency and its accurate content, the peak area of La 3d_{3/2} was subtracted from the Ni 3p_{3/2}. The two Ni 2p_{3/2} peaks with a binding energy of 854.18 and 855.70 eV are attributed to the surface Ni²⁺ and Ni³⁺ species on the LNO, respectively. The binding energies of Ni³⁺ in LNFCO- x ($x = 0.4, 0.5$, and 0.6) showed a gradual increase (856.20, 856.47, and 856.75 eV), which indicates the slight oxidation of Ni³⁺ species. However, the signal ratio of Ni³⁺/Ni²⁺ diminishes with the substitution of Co/Fe, indicating that Ni³⁺ is occupied by the Fe and Co ions. The Fe 2p_{3/2} region (Figure 5c) is stretched till 721 eV, which indicates the presence of Fe valency greater than 3+, Fe^{3+Δ}

Table 1. List of the Bond Energies of O 1s, Ni 2p_{3/2}, Co 2p_{3/2}, and Fe 2p_{3/2} and the Signal Fraction of Ni³⁺/Ni²⁺, Fe^{3+Δ}/Fe³⁺, and Co³⁺/Co²⁺

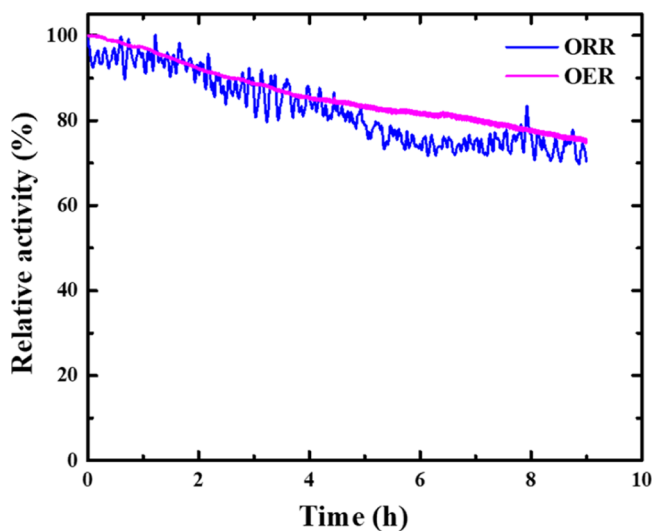
LNFCO- <i>x</i> , <i>x</i> =	O 1s	Ni 2p _{3/2}	Co 2p _{3/2}	Fe 2p _{3/2}	O _{ads} /O _{lat}	Ni ³⁺ /Ni ²⁺	Fe ^{3+Δ} /Fe ³⁺	Co ³⁺ /Co ²⁺
0.0	528.51	854.18			1.80	0.63		
	529.82	855.70						
	531.38							
	533.05							
0.4	528.56	854.38	780.1	710.3	1.38	0.27	2.84	0.20
	529.72	856.20	782.9	714.7				
	531.32							
	533.09							
0.5	528.68	854.14	780.6	711.1	1.31	0.21	1.39	0.35
	529.87	856.47	782.6	715.3				
	531.33							
	532.69							
0.6	528.89	854.46	780.2	711.2	1.37	0.24	1.28	0.42
	529.90	856.75	782.8	714.1				
	531.50							
	532.72							

(~714–715 eV) along with the Fe³⁺ (~710–711 eV) in LNFCO-*x* (*x* = 0.4, 0.5, and 0.6). The peaks related to Co³⁺ and Co²⁺ appeared at their characteristic positions without significant shifts (Figure 5d). Table 1 lists the binding energies of O 1s, Ni 2p_{3/2}, Co 2p_{3/2}, and Fe 2p_{3/2} with the signal ratios of Ni³⁺/Ni²⁺, Fe^{3+Δ}/Fe³⁺, and Co³⁺/Co²⁺.

DFT calculations have revealed that the deprotonation of *OH to *O is the rds in the OER of LNO.⁴² From the molecular orbital theory considerations and experimental observations, the e_g-orbital filling is found to be the most suitable descriptor for both ORR and OER activities of perovskite-based catalysts.^{34,57} Also, the highest activities were found for the catalysts with e_g-orbital filling close to 1.2. The catalysts with e_g > 1 resulted in too strong binding energy of *OH⁻, whereas e_g < 1 led to too weak binding energy. The e_g-orbital filling for LNO is reported to be greater than unity, and it is found to be sensitive to the ratio of surface Ni valences (Ni³⁺: t_{2g}⁶e_g¹ and Ni²⁺: t_{2g}⁶e_g²) Ni³⁺/Ni²⁺.⁷¹ Therefore, strategies that are conducive to the e_g-orbital filling of LNO could enhance the oxygen redox activity. The Ni³⁺/Ni²⁺, Fe^{3+Δ}/Fe³⁺, and Co³⁺/Co²⁺ ratios suggest that the surface of LNFCO-0.6 is largely populated with Ni²⁺, Co³⁺, and Fe^{3+Δ} oxidation states. The low Ni³⁺/Ni²⁺ (1/1.57) ratio indicates the higher e_g-orbital filling than the ideal (e_g = 1.2) for the OER. The enrichment of the surface with Fe^{3+Δ} (~t_{2g}³e_g¹) and Co³⁺ (t_{2g}⁶e_g⁰) at the Ni³⁺ (t_{2g}⁶e_g¹) state can bring down the e_g-orbital filling closer to 1.2, which enables the catalytic activity of LNFCO-0.5 in the ORR and OER. The oxygen redox reactions of LNO involve the active Ni^{3+/4+} redox couple. The fully occupied Ni t_{2g}⁶ and O 2p⁶ orbitals experience large electron–electron repulsions (Ni^{3+/4+}–O–Ni^{3+/4+}), which inhibit the formation of the Ni⁴⁺ state.⁴² The presence of partially oxidized Ni³⁺ and Fe^{3+Δ} in the LNFCO-0.5 reduces such electron–electron repulsions and promotes the Ni^{3+/4+} redox activity. The O-K edge X-ray absorption spectra of Fe-substituted LNO thin films revealed that the presence of Fe⁴⁺ also reduces the charge-transfer energy by creating unoccupied e_g states below the conduction band minimum.^{42,43} This electronic structure favors the electron transfer from Ni³⁺ to O²⁻ and O²⁻ to Fe⁴⁺. Similarly, the presence of Fe^{3+Δ} and Co³⁺ oxidation states plays a vital role in optimizing the e_g-orbital filling and creating unoccupied e_g states, which enables the

oxygen redox activity of LNFCO-0.5. The synergistic effect of the Fe–Co presence in perovskite oxides was reported. Yamada et al. studied the OER activity of Ca₂B₂O₅ (B = Fe or Co and FeCo) and CaBO₃ (B = Fe, Co, and Fe_{0.5}Co_{0.5}) perovskites and found the beneficial synergistic effect on OER activities by the Fe–Co mixed oxides.⁴⁵ However, the e_g-orbital filling of CaCoO₃, CaFeO₃, and CaFe_{0.5}Co_{0.5}O₃ is nearly unity. Therefore, the charge-transfer energy was preferred as a suitable descriptor over the e_g-orbital filling.

3.5. Stability Test. The structural stability during the electrochemical processes directly resembles the durability of electrochemical energy storage and conversion devices such as fuel cells and metal–air batteries. The stability tests for LNFCO-0.5 in the ORR and OER were carried out using chronoamperometry for 9 h at 0.68 (–1 mA cm⁻²) and 1.64 V versus RHE (10 mA cm⁻²) in 1 M KOH, respectively (Figure 6). The ORR activity of LNFCO-0.5 was almost constant from 6 to 9 h and retains 74% of its value. The OER activity exhibited a linear decrease and retained 75% of its value at 9 h.

**Figure 6.** Chronoamperometric response of LNFCO-0.5 in the ORR and OER at 0.68 (–1 mA cm⁻²) and 1.64 V versus RHE (10 mA cm⁻²) in 1 M KOH, respectively.

We have examined the surface $\text{Ni}^{3+/2+}$ redox site before and after 9 h of the ORR and OER to understand the surface valency changes. Figure S14 shows the CVs of LNFCO-0.5 before and after the stability test. The prominent increment in the $\text{Ni}^{3+/2+}$ redox peak indicates the Ni-rich surface of LNFCO-0.5 after 9 h of stability test.³⁶ During the OER, the $\text{Ni}^{3+/2+}$ redox peak also increased and slightly broadened, which shows possible surface degradation. The amount of Ni, Fe, and Co leaked into the electrolyte was quantified using ICP-OES analysis. The quantity of Co lost into the electrolyte was 0.0002 and 0.002 mg L⁻¹ during the ORR and OER, respectively. The Fe and Ni contents were beyond the detectable level of the ICP-OES instrument. To further understand the loss in ORR and OER activities, we have characterized the XRD and HR-TEM of post-OER and -ORR catalysts. The XRD reflections of (012), (110), and (104) were shifted to higher angles in both the catalysts, and all other reflections were retained, which indicates the bulk structural changes (lattice parameters decreased) during the ORR and OER (Figure S15a,b). The HR-TEM image shows the NiO particles with a size of ~15 nm on the post-ORR catalyst, which corroborates the enhanced $\text{Ni}^{3+/2+}$ redox peak during the ORR. Figure S16a shows the surface of LNFCO-0.5 after the ORR. The protruded spherical particles are identified as NiO by the presence of (311) planes ($d(311) = 0.26$ nm).³⁶ Figure S16b shows the amorphous nature of LNFCO-0.5 after the OER. The results demonstrate that the loss of the lattice B-site (Ni as NiO) can be ascertained to the ORR decay. The destruction of crystallinity of the catalyst could be the result of the dissolution of $\text{Co}^{3+}/\text{Co}^{2+}$ and/or $\text{Fe}^{3+\Delta}/\text{Fe}^{3+}$, which in turn reflects deterioration of the OER activity. The XPS data of LNFCO-0.5 after 9 h of ORR and OER are shown in Figure S17a–d. There are no detectable Fe and Co XPS peaks in Figure S17c,d. Overall, not only the BI but also the stability of LNFCO-0.5 was improved compared to that of LNO and $\text{La}_{1-x}\text{NiO}_3$. Therefore, we believe that LNFCO-0.5 could be a potential catalyst for rechargeable metal–air batteries. As a proof of concept, we have fabricated a flexible Zn–air battery as presented in Figure S18a. The battery shows an open-circuit potential (OCV) of 1.236 V. As shown in Figure S18b, the battery holds the OCV (1.228 V) nearly stable even after bending at 80°. Two such batteries were connected in series to glow a 2 V LED bulb (Figure S18c). Further in-depth studies on the higher valences of transition metals and device engineering are suggested to fabricate potential flexible Zn–air batteries.

4. CONCLUSIONS

We employed DFT calculations to identify the suitable doping concentrations of Fe and Co for Ni in LNO to attain the suitable electronic structure for improved BI of oxygen redox reactions. A simple and facile sol–gel method followed by a pyrolysis step was used for the synthesis of LNFCO- x ($x = 0.0, 0.4, 0.5,$ and 0.6). The presence of $\text{Fe}^{3+\Delta}$ - and Co^{3+} -sites promoted the oxygen redox activity. Among the evaluated catalysts, LNFCO-0.5 has exhibited the lowest overpotential and the highest charge transfer kinetics in oxygen redox reactions. Overall, a 90 mV lower overpotential was observed in oxygen redox activity of LNFCO-0.5 compared to that of the pristine LaNiO_3 . The mass activity of LNFCO-0.5 in the ORR (at 0.7 V vs RHE) and OER (1.60 V vs RHE) was calculated to be 2.5 and 2.13 times higher than that of the LaNiO_3 , respectively. The BI (potential difference between the

oxygen evolution at a current density of 10 mA cm⁻² and the oxygen reduction at a current density of -1 mA cm⁻²) of LNFCO-0.5 was found to be 0.98, which is superior to that of LaNiO_3 (1.33). The surface cation distribution of $\text{Fe}^{3+\Delta}$ -, Co^{3+} -, and partially oxidized Ni^{3+} -sites could shift the e_g -orbital filling of LNO ($e_g > 1.2$) toward ideal ($e_g = 1.2$). Our study highlights the importance of $\text{Fe}^{3+\Delta}$ - and Co^{3+} -sites in LNO to develop efficient and earth-abundant nonprecious metal catalysts for fuel cells and rechargeable metal–air batteries.

■ ASSOCIATED CONTENT

SI Supporting Information

The Supporting Information is available free of charge at <https://pubs.acs.org/doi/10.1021/acsaem.1c02871>.

SEM and HR-TEM images and photographs (PDF)

■ AUTHOR INFORMATION

Corresponding Author

Raman Sankar – Institute of Physics, Academia Sinica, Taipei 11529, Taiwan; orcid.org/0000-0003-4702-2517;
Email: sankarraman@gate.sinica.edu.tw

Authors

Anjaiah Sheelam – Institute of Physics, Academia Sinica, Taipei 11529, Taiwan; orcid.org/0000-0002-1099-8439
Sakthipriya Balu – Department of Mechanical Engineering, National Taiwan University of Science and Technology, Taipei 10607, Taiwan
Adil Muneeb – Department of Mechanical Engineering, National Taiwan University of Science and Technology, Taipei 10607, Taiwan
Khasim Saheb Bayikadi – Institute of Physics, Academia Sinica, Taipei 11529, Taiwan
Dhenadhayalan Namasivayam – Institute of Atomic and Molecular Sciences, Taipei 10617, Taiwan; orcid.org/0000-0003-4494-5746
Erakulan E. Siddharthan – SRM University, Tirupati, Andhra Pradesh 522240, India
Arif I. Inamdar – Institute of Chemistry, Academia Sinica, Taipei 11529, Taiwan; orcid.org/0000-0003-3021-0837
Ranjit Thapa – SRM University, Tirupati, Andhra Pradesh 522240, India
Ming-Hsi Chiang – Institute of Chemistry, Academia Sinica, Taipei 11529, Taiwan; orcid.org/0000-0002-7632-9369
Song-Jeng Isaac Huang – Department of Mechanical Engineering, National Taiwan University of Science and Technology, Taipei 10607, Taiwan

Complete contact information is available at:
<https://pubs.acs.org/doi/10.1021/acsaem.1c02871>

Author Contributions

A.S.: conceptualization, data curation, analysis, writing, reviewing, and editing; S.B.: data curation; A.M.: data curation; B.K.S.: data curation; D.N.: data curation; E.E.S.: data curation, analysis, and writing; A.I.: data curation; R.T.: validation, analysis, and writing; M.-H.C.: validation and reviewing; S.-J.H.: validation and reviewing; R.S.: fund acquisition, validation, analysis, writing, reviewing, and editing.

Notes

The authors declare no competing financial interest.

ACKNOWLEDGMENTS

R.S. acknowledges the financial support provided by the Ministry of Science and Technology in Taiwan under Project No. MOST-110-2112-M-001-065-MY3 and Academia Sinica budget of AS-iMATE-112-12. A.S. thanks Dr. Raju Kalivanan for his help in conducting low-temperature resistivity measurements under magnetic fields.

REFERENCES

- (1) Khan, N.; Dilshad, S.; Khalid, R.; Kalair, A. R.; Abas, N. Review of energy storage and transportation of energy. *Energy Storage* **2019**, *1*, No. e49.
- (2) Staffell, I.; Scamman, D.; Velazquez Abad, A.; Balcombe, P.; Dodds, P. E.; Ekins, P.; Shah, N.; Ward, K. R. The role of hydrogen and fuel cells in the global energy system. *Energy Environ. Sci.* **2019**, *12*, 463–491.
- (3) Zhang, J.; Zhou, Q.; Tang, Y.; Zhang, L.; Li, Y. Zinc-air batteries: are they ready for prime time? *Chem. Sci.* **2019**, *10*, 8924–8929.
- (4) Meng, F.-L.; Liu, K.-H.; Zhang, Y.; Shi, M.-M.; Zhang, X.-B.; Yan, J.-M.; Jiang, Q. Recent Advances toward the Rational Design of Efficient Bifunctional Air Electrodes for Rechargeable Zn–Air Batteries. *Small* **2018**, *14*, 1703843.
- (5) Song, J.; Wei, C.; Huang, Z.-F.; Liu, C.; Zeng, L.; Wang, X.; Xu, Z. J. A review on fundamentals for designing oxygen evolution electrocatalysts. *Chem. Soc. Rev.* **2020**, *49*, 2196–2214.
- (6) Gómez-Marín, A. M.; Ticianelli, E. A. A reviewed vision of the oxygen reduction reaction mechanism on Pt-based catalysts. *Curr. Opin. Electrochem.* **2018**, *9*, 129–136.
- (7) Nørskov, J. K.; Rossmeisl, J.; Logadottir, A.; Lindqvist, L.; Kitchin, J. R.; Bligaard, T.; Jónsson, H. Origin of the Overpotential for Oxygen Reduction at a Fuel-Cell Cathode. *J. Phys. Chem. B* **2004**, *108*, 17886–17892.
- (8) Fabbri, E.; Haberer, A.; Waltar, K.; Kötz, R.; Schmidt, T. J. Developments and perspectives of oxide-based catalysts for the oxygen evolution reaction. *Catal. Sci. Technol.* **2014**, *4*, 3800–3821.
- (9) Sui, S.; Wang, X.; Zhou, X.; Su, Y.; Riffat, S.; Liu, C.-j. A comprehensive review of Pt electrocatalysts for the oxygen reduction reaction: Nanostructure, activity, mechanism and carbon support in PEM fuel cells. *J. Mater. Chem. A* **2017**, *5*, 1808–1825.
- (10) McCrory, C. C. L.; Jung, S.; Peters, J. C.; Jaramillo, T. F. Benchmarking Heterogeneous Electrocatalysts for the Oxygen Evolution Reaction. *J. Am. Chem. Soc.* **2013**, *135*, 16977–16987.
- (11) Wu, D.; Shen, X.; Pan, Y.; Yao, L.; Peng, Z. Platinum Alloy Catalysts for Oxygen Reduction Reaction: Advances, Challenges and Perspectives. *ChemNanoMat* **2020**, *6*, 32–41.
- (12) Ren, X.; Lv, Q.; Liu, L.; Liu, B.; Wang, Y.; Liu, A.; Wu, G. Current progress of Pt and Pt-based electrocatalysts used for fuel cells. *Sustainable Energy Fuels* **2020**, *4*, 15–30.
- (13) Takeguchi, T.; Yamanaka, T.; Takahashi, H.; Watanabe, H.; Kuroki, T.; Nakanishi, H.; Orikasa, Y.; Uchimoto, Y.; Takano, H.; Ohguri, N.; Matsuda, M.; Murota, T.; Uosaki, K.; Ueda, W. Layered Perovskite Oxide: A Reversible Air Electrode for Oxygen Evolution/Reduction in Rechargeable Metal-Air Batteries. *J. Am. Chem. Soc.* **2013**, *135*, 11125–11130.
- (14) Sun, S.; Zhou, X.; Cong, B.; Hong, W.; Chen, G. Tailoring the d-Band Centers Endows (Ni_xFe_{1-x})₂P Nanosheets with Efficient Oxygen Evolution Catalysis. *ACS Catal.* **2020**, *10*, 9086–9097.
- (15) Cui, H.; Guo, Y.; Ma, W.; Zhou, Z. 2D Materials for Electrochemical Energy Storage: Design, Preparation, and Application. *ChemSusChem* **2020**, *13*, 1155–1171.
- (16) Lin, L.; Zhu, Q.; Xu, A.-W. Noble-Metal-Free Fe–N/C Catalyst for Highly Efficient Oxygen Reduction Reaction under Both Alkaline and Acidic Conditions. *J. Am. Chem. Soc.* **2014**, *136*, 11027–11033.
- (17) Sheelam, A.; Ramanujam, K. Nitrogen Functionalized Few Layer Graphene Derived from Metal-Organic Compound: A Catalyst for Oxygen Reduction Reaction. *Electrochim. Acta* **2016**, *216*, 457–466.
- (18) Karthikayini, M. P.; Wang, G.; Bhojeb, P. A.; Sheelam, A.; Ramani, V. K.; Priolkar, K. R.; Raman, R. K. Effect of Protonated Amine Molecules on the Oxygen Reduction Reaction on Metal-Nitrogen-Carbon-Based Catalysts. *Electrocatalysis* **2017**, *8*, 74–85.
- (19) Sheelam, A.; Ramanujam, K. Metal-Organic Complexes, [Co(bpy)₃](NO₃)₂ and [Co(bpy)₂NO₃](NO₃)·5H₂O, for Oxygen Reduction Reaction. *J. Electrochem. Soc.* **2017**, *164*, F1022–F1029.
- (20) Sheelam, A.; Mandal, S.; Thippiani, T.; Ramkumar, V.; Ramanujam, K. Carbon-supported Co(III) dimer for oxygen reduction reaction in alkaline medium. *Ionics* **2016**, *22*, 2183–2194.
- (21) Sheelam, A.; Ramanujam, K. Iron(III) chloride-benzotriazole adduct for oxygen reduction reaction in alkaline medium. *Int. J. Hydrogen Energy* **2018**, *43*, 4754–4762.
- (22) Sheelam, A.; Sankar, R. Carbon-supported cobalt (III) complex for direct reduction of oxygen in alkaline medium. *Int. J. Hydrogen Energy* **2020**, *45*, 24738–24748.
- (23) Mani, P.; Sheelam, A.; Das, S.; Wang, G.; Ramani, V. K.; Ramanujam, K.; Pati, S. K.; Mandal, S. Cobalt-Based Coordination Polymer for Oxygen Reduction Reaction. *ACS Omega* **2018**, *3*, 3830–3834.
- (24) Mani, P.; Sheelam, A.; Karthik, P. E.; Sankar, R.; Ramanujam, K.; Mandal, S. Nickel-Based Hybrid Material for Electrochemical Oxygen Redox Reactions in an Alkaline Medium. *ACS Appl. Energy Mater.* **2020**, *3*, 6408–6415.
- (25) Peña, M. A.; Fierro, J. L. G. Chemical Structures and Performance of Perovskite Oxides. *Chem. Rev.* **2001**, *101*, 1981–2018.
- (26) Ji, Q.; Bi, L.; Zhang, J.; Cao, H.; Zhao, X. S. The role of oxygen vacancies of ABO₃ perovskite oxides in the oxygen reduction reaction. *Energy Environ. Sci.* **2020**, *13*, 1408–1428.
- (27) Fresno, F.; Jana, P.; Reñones, P.; Coronado, J. M.; Serrano, D. P.; de la Peña O’Shea, V. A. CO₂ reduction over NaNbO₃ and NaTaO₃ perovskite photocatalysts. *Photochem. Photobiol. Sci.* **2017**, *16*, 17–23.
- (28) Ciambelli, P.; Cimino, S.; De Rossi, S.; Lisi, L.; Minelli, G.; Porta, P.; Russo, G. AFeO₃ (A=La, Nd, Sm) and LaFe_{1-x}Mg_xO₃ perovskites as methane combustion and CO oxidation catalysts: structural, redox and catalytic properties. *Appl. Catal., B* **2001**, *29*, 239–250.
- (29) Huang, H.-L.; Jeng, H.-T. Orbital ordering and magnetism in layered Perovskite Ruthenate Sr₂RuO₄. *Sci. Rep.* **2020**, *10*, 7089.
- (30) He, H.; Yang, Z.; Xu, Y.; Smith, A. T.; Yang, G.; Sun, L. Perovskite oxides as transparent semiconductors: a review. *Nano Convergence* **2020**, *7*, 32.
- (31) Gholizadeh, A. The effects of A/B-site substitution on structural, redox and catalytic properties of lanthanum ferrite nanoparticles. *J. Mater. Res. Technol.* **2019**, *8*, 457–466.
- (32) Sun, C.; Alonso, J. A.; Bian, J. Recent Advances in Perovskite-Type Oxides for Energy Conversion and Storage Applications. *Adv. Energy Mater.* **2021**, *11*, 2000459.
- (33) Seo, M. H.; Park, H. W.; Lee, D. U.; Park, M. G.; Chen, Z. Design of Highly Active Perovskite Oxides for Oxygen Evolution Reaction by Combining Experimental and ab Initio Studies. *ACS Catal.* **2015**, *5*, 4337–4344.
- (34) Suntivich, J.; Hong, W. T.; Lee, Y.-L.; Rondinelli, J. M.; Yang, W.; Goodenough, J. B.; Dabrowski, B.; Freeland, J. W.; Shao-Horn, Y. Estimating Hybridization of Transition Metal and Oxygen States in Perovskites from O K-edge X-ray Absorption Spectroscopy. *J. Phys. Chem. C* **2014**, *118*, 1856–1863.
- (35) Suntivich, J.; Gasteiger, H. A.; Yabuuchi, N.; Nakanishi, H.; Goodenough, J. B.; Shao-Horn, Y. Design principles for oxygen-reduction activity on perovskite oxide catalysts for fuel cells and metal–air batteries. *Nat. Chem.* **2011**, *3*, 546–550.
- (36) Qiu, Y.; Gao, R.; Yang, W.; Huang, L.; Mao, Q.; Yang, J.; Sun, L.; Hu, Z.; Liu, X. Understanding the Enhancement Mechanism of A-Site-Deficient La_xNiO₃ as an Oxygen Redox Catalyst. *Chem. Mater.* **2020**, *32*, 1864–1875.
- (37) Liu, J.; Jia, E.; Wang, L.; Stoerzinger, K. A.; Zhou, H.; Tang, C. S.; Yin, X.; He, X.; Bousquet, E.; Bowden, M. E.; Wee, A. T. S.; Chambers, S. A.; Du, Y. Tuning the Electronic Structure of LaNiO₃

through Alloying with Strontium to Enhance Oxygen Evolution Activity. *Adv. Sci.* **2019**, *6*, 1901073.

(38) Hong, W. T.; Stoerzinger, K. A.; Lee, Y.-L.; Giordano, L.; Grimaud, A.; Johnson, A. M.; Hwang, J.; Crumlin, E. J.; Yang, W.; Shao-Horn, Y. Charge-transfer-energy-dependent oxygen evolution reaction mechanisms for perovskite oxides. *Energy Environ. Sci.* **2017**, *10*, 2190–2200.

(39) Neagu, D.; Oh, T.-S.; Miller, D. N.; Ménard, H.; Bukhari, S. M.; Gamble, S. R.; Gorte, R. J.; Vohs, J. M.; Irvine, J. T. S. Nano-socketed nickel particles with enhanced coking resistance grown in situ by redox exsolution. *Nat. Commun.* **2015**, *6*, 8120.

(40) Zhu, Y.; Zhou, W.; Yu, J.; Chen, Y.; Liu, M.; Shao, Z. Enhancing Electrocatalytic Activity of Perovskite Oxides by Tuning Cation Deficiency for Oxygen Reduction and Evolution Reactions. *Chem. Mater.* **2016**, *28*, 1691–1697.

(41) Wang, H.; Chen, X.; Huang, D.; Zhou, M.; Ding, D.; Luo, H. Cation Deficiency Tuning of LaCoO₃ Perovskite as Bifunctional Oxygen Electrocatalyst. *ChemCatChem* **2020**, *12*, 2768–2775.

(42) Fu, G.; Li, W.; Zhang, J. Y.; Li, M.; Li, C.; Li, N.; He, Q.; Xi, S.; Qi, D.; MacManus-Driscoll, J. L.; Cheng, J.; Zhang, K. H. Facilitating the Deprotonation of OH to O through Fe⁴⁺-Induced States in Perovskite LaNiO₃ Enables a Fast Oxygen Evolution Reaction. *Small* **2021**, *17*, 2006930.

(43) Shen, Z.; Zhuang, Y.; Li, W.; Huang, X.; Oropeza, F. E.; Hensen, E. J. M.; Hofmann, J. P.; Cui, M.; Tadich, A.; Qi, D.; Cheng, J.; Li, J.; Zhang, K. H. L. Increased activity in the oxygen evolution reaction by Fe⁴⁺-induced hole states in perovskite La_{1-x}Sr_xFeO₃. *J. Mater. Chem. A* **2020**, *8*, 4407–4415.

(44) Huang, S.-J.; Muneeb, A.; Sabhapathy, P.; Sheelam, A.; Bayikadi, K. S.; Sankar, R. Tailoring the Co⁴⁺/Co³⁺ active sites in a single perovskite as a bifunctional catalyst for the oxygen electrode reactions. *Dalton Trans.* **2021**, *50*, 7212–7222.

(45) Yamada, I.; Kinoshita, M.; Oda, S.; Tsukasaki, H.; Kawaguchi, S.; Oka, K.; Mori, S.; Ikeno, H.; Yagi, S. Enhanced Catalytic Activity and Stability of the Oxygen Evolution Reaction on Tetravalent Mixed Metal Oxide. *Chem. Mater.* **2020**, *32*, 3893–3903.

(46) Yagi, S.; Yamada, I.; Tsukasaki, H.; Seno, A.; Murakami, M.; Fujii, H.; Chen, H.; Umezawa, N.; Abe, H.; Nishiyama, N.; et al. Covalency-reinforced oxygen evolution reaction catalyst. *Nat. Commun.* **2015**, *6*, 8249.

(47) Woodward, P. M.; Cox, D. E.; Moshopoulou, E.; Sleight, A. W.; Morimoto, S. Structural studies of charge disproportionation and magnetic order in CaFeO₃. *Phys. Rev. B* **2000**, *62*, 844–855.

(48) Denis Romero, F.; Shimakawa, Y. Charge transitions in perovskite oxides containing unusually high-valent Fe. *Chem. Commun.* **2019**, *55*, 3690–3696.

(49) May, K. J.; Carlton, C. E.; Stoerzinger, K. A.; Risch, M.; Suntivich, J.; Lee, Y.-L.; Grimaud, A.; Shao-Horn, Y. Influence of Oxygen Evolution during Water Oxidation on the Surface of Perovskite Oxide Catalysts. *J. Phys. Chem. Lett.* **2012**, *3*, 3264–3270.

(50) Kresse, G.; Furthmüller, J. Efficiency of ab-initio total energy calculations for metals and semiconductors using a plane-wave basis set. *Comput. Mater. Sci.* **1996**, *6*, 15–50.

(51) Giannozzi, P.; Baroni, S.; Bonini, N.; Calandra, M.; Car, R.; Cavazzoni, C.; Ceresoli, D.; Chiarotti, G. L.; Cococcioni, M.; Dabo, I.; et al. QUANTUM ESPRESSO: a modular and open-source software project for quantum simulations of materials. *J. Phys. Condens. Matter.* **2009**, *21*, 395502.

(52) Blöchl, P. E. Projector augmented-wave method. *Phys. Rev. B* **1994**, *50*, 17953–17979.

(53) Perdew, J. P.; Burke, K.; Ernzerhof, M. Generalized Gradient Approximation Made Simple. *Phys. Rev. Lett.* **1996**, *77*, 3865–3868.

(54) Paulus, U. A.; Schmidt, T. J.; Gasteiger, H. A.; Behm, R. J. Oxygen reduction on a high-surface area Pt/Vulcan carbon catalyst: a thin-film rotating ring-disk electrode study. *J. Electroanal. Chem.* **2001**, *495*, 134–145.

(55) Fan, X.; Liu, J.; Song, Z.; Han, X.; Deng, Y.; Zhong, C.; Hu, W. Porous nanocomposite gel polymer electrolyte with high ionic

conductivity and superior electrolyte retention capability for long-cycle-life flexible zinc–air batteries. *Nano Energy* **2019**, *56*, 454–462.

(56) Pettersson, L. G. M.; Nilsson, A. A Molecular Perspective on the d-Band Model: Synergy Between Experiment and Theory. *Top. Catal.* **2014**, *57*, 2–13.

(57) Zhang, D.; Song, Y.; Du, Z.; Wang, L.; Li, Y.; Goodenough, J. B. Active LaNi_{1-x}Fe_xO₃ bifunctional catalysts for air cathodes in alkaline media. *J. Mater. Chem. A* **2015**, *3*, 9421–9426.

(58) Suntivich, J.; May, K. J.; Gasteiger, H. A.; Goodenough, J. B.; Shao-Horn, Y. A Perovskite Oxide Optimized for Oxygen Evolution Catalysis from Molecular Orbital Principles. *Science* **2011**, *334*, 1383–1385.

(59) Nørskov, J. K.; Abild-Pedersen, F.; Studt, F.; Bligaard, T. Density functional theory in surface chemistry and catalysis. *Proc. Natl. Acad. Sci. U. S. A.* **2011**, *108*, 937.

(60) Shannon, R. D. Revised effective ionic radii and systematic studies of interatomic distances in halides and chalcogenides. *Acta Crystallogr., Sect. A: Cryst. Phys., Diffr., Theor. Gen. Crystallogr.* **1976**, *32*, 751–767.

(61) Fowlie, J.; Gibert, M.; Tieri, G.; Gloter, A.; Íñiguez, J.; Filippetti, A.; Catalano, S.; Gariglio, S.; Schober, A.; Guennou, M.; Kreisel, J.; Stéphan, O.; Triscone, J.-M. Conductivity and Local Structure of LaNiO₃ Thin Films. *Adv. Mater.* **2017**, *29*, 1605197.

(62) Tai, X. Y.; Zhakeyev, A.; Wang, H.; Jiao, K.; Zhang, H.; Xuan, J. Accelerating Fuel Cell Development with Additive Manufacturing Technologies: State of the Art, Opportunities and Challenges. *Fuel Cells* **2019**, *19*, 636–650.

(63) Bae, D.; Seger, B.; Vesborg, P. C. K.; Hansen, O.; Chorkendorff, I. Strategies for stable water splitting via protected photoelectrodes. *Chem. Soc. Rev.* **2017**, *46*, 1933–1954.

(64) Chen, B.; Wang, J.; Yang, T.; Cai, Y.; Zhang, C.; Chan, S. H.; Yu, Y.; Tu, Z. Carbon corrosion and performance degradation mechanism in a proton exchange membrane fuel cell with dead-ended anode and cathode. *Energy* **2016**, *106*, 54–62.

(65) Zhong, G.; Xu, S.; Liu, L.; Zheng, C. Z.; Dou, J.; Wang, F.; Fu, X.; Liao, W.; Wang, H. Effect of Experimental Operations on the Limiting Current Density of Oxygen Reduction Reaction Evaluated by Rotating-Disk Electrode. *ChemElectroChem* **2020**, *7*, 1107–1114.

(66) Wang, H.; Xu, W.; Richins, S.; Liaw, K.; Yan, L.; Zhou, M.; Luo, H. Polymer-assisted approach to LaCo_{1-x}Ni_xO₃ network nanostructures as bifunctional oxygen electrocatalysts. *Electrochim. Acta* **2019**, *296*, 945–953.

(67) Miao, H.; Wu, X.; Chen, B.; Wang, Q.; Wang, F.; Wang, J.; Zhang, C.; Zhang, H.; Yuan, J.; Zhang, Q. A-site deficient/excessive effects of LaMnO₃ perovskite as bifunctional oxygen catalyst for zinc-air batteries. *Electrochim. Acta* **2020**, *333*, 135566.

(68) Qian, J.; Bai, X.; Xi, S.; Xiao, W.; Gao, D.; Wang, J. Bifunctional Electrocatalytic Activity of Nitrogen-Doped NiO Nanosheets for Rechargeable Zinc–Air Batteries. *ACS Appl. Mater. Interfaces* **2019**, *11*, 30865–30871.

(69) Lambert, T. N.; Vigil, J. A.; White, S. E.; Davis, D. J.; Limmer, S. J.; Burton, P. D.; Coker, E. N.; Beechem, T. E.; Brumbach, M. T. Electrodeposited Ni_xCo_{3-x}O₄ nanostructured films as bifunctional oxygen electrocatalysts. *Chem. Commun.* **2015**, *51*, 9511–9514.

(70) Fu, G.; Cui, Z.; Chen, Y.; Li, Y.; Tang, Y.; Goodenough, J. B. Ni₃Fe–N Doped Carbon Sheets as a Bifunctional Electrocatalyst for Air Cathodes. *Adv. Energy Mater.* **2017**, *7*, 1601172.

(71) Guo, Q.; Li, X.; Wei, H.; Liu, Y.; Li, L.; Yang, X.; Zhang, X.; Liu, H.; Lu, Z. Sr, Fe Co-doped Perovskite Oxides With High Performance for Oxygen Evolution Reaction. *Front. Chem.* **2019**, *7*, 1–8.